Application of molecular dynamics to the study of hydrogen embrittlement in Ni-Cr-Fe alloys

Richard W. Smith* and Gary S. Was
Department of Nuclear Engineering, The University of Michigan, Ann Arbor, Michigan 48109
(Received 4 May 1989)

Molecular dynamics and the embedded-atom method (EAM) have been applied to the study of intergranular hydrogen embrittlement in Ni-based alloys. A new technique was developed for constructing EAM functions from experimental data on binary systems. The technique allows one to express experimental quantities of the binary alloy in terms of EAM functions for each constituent element, and then to fine tune the parameters for one of the elements to fit the experimental data. The method was used to construct EAM functions for H and for the Ni-Cr-Fe system. The functions were then used in dynamic simulations of grain boundaries to study the effect of H on their stress-strain–fracture behavior. The simulations suggest that hydrogen-embrittlement susceptibility is strongly linked to grain-boundary structure. Boundaries possessing large gaps and structural irregularities are affected adversely, while boundaries lacking these defects are resistant to embrittlement. The results of the study are discussed in terms of the influence of the simulation methodology on the observed grain-boundary fracture behavior of Ni-Cr-Fe alloys as a function of boundary type, boundary structure, and hydrogen content.

I. INTRODUCTION

It has long been recognized that the introduction of atomic hydrogen into metallic alloys causes the metal to become embrittled. The embrittlement is often manifested by a significant increase in the ultimate tensile strength and work-hardening rate and a reduction in the strain to fracture as well as a shift in the fracture mode from transgranular to intergranular.[1] Due to the engineering importance of this problem, a great deal of research has been directed at determining the conditions under which embrittlement occurs and in quantifying the effects. Studies have shown that in many materials, intergranular fracture due to hydrogen occurs in a brittle fashion within the grain-boundary plane,[2–4] while in other alloys embrittlement takes place in matrix regions adjacent to the boundary by plastic mechanisms.[5–8] In either event, the observed embrittlement is related to the amount of hydrogen segregated to the boundary, and matrix hydrogen does not appear to cause a problem. In the Ni-based alloys such as Inconel Alloy 600 (Ni-16Cr-9Fe), (Inconel is a registered trademark of Huntington Alloys, Inc.), fracture has been observed to occur within the boundary plane, with the degree of embrittlement being closely tied to the presence of additional segragated species such as phosphorus and sulfur.[2,6,9] In addition, grain-boundary embrittlement has been correlated to certain classes of grain-boundary (GB) structures.[10–12]

On the other hand, very little is known about the actual mechanisms by which embrittlement occurs. It is not known whether the effect of hydrogen is simply to reduce the cohesion across the boundary or if more complicated plastic processes involving dislocation generation and transport are at play. In addition, it is not known whether the factors which influence embrittlement are affecting a single mechanism or altering the prevalence among competing processes.

In order to study the problem in detail, it is necessary to use computer-simulation techniques which can investigate events on a much finer space and time scale than can be reached with presently available experimental techniques. The simulation techniques most readily applied to the study of fracture and embrittlement on the atomic scale are molecular dynamics (MD), and quantum-chemical methods. With molecular dynamics, one assembles an atomistic configuration of perhaps 100 to 10 000 atoms in a computational cell and then follows their collective motion, subject to prescribed interatomic force laws. With quantum-chemical methods, one starts with a small cluster of atoms ($\simeq 10$), the positions of which are frozen in space. Approximate solutions to Schrödinger's equation are then applied to determine the distribution of electron density throughout the cluster. The resulting distribution is used to analyze the bonding characteristics of the cluster.

Quantum-chemical techniques have been used extensively by Briant and Messmer[13–17] to study the interaction between impurity atoms and metallic species at grain boundaries. In these studies, the Slater-Johnson $X\alpha$ scattered-wave method[18] has been applied to compute the electron density throughout small clusters of atoms (typically 4 to 12), arranged in a structure thought to be representative of the simplest configurations attained by atoms spanning a grain-boundary plane. These authors and their co-workers have applied the method to the study of S in Ni,[13] H in Fe,[16] P in both Fe and Cr,[14] Sb in both Fe and Ni,[15] C in Fe,[17] and B in Ni.[17] Although potentially more accurate, quantum-chemical methods are almost exclusively limited to static structures due to computational expense.

In order to study the dynamic processes of fracture, it is necessary to use molecular dynamics and therefore some approximate treatment of the various interatomic forces. Molecular dynamics has been applied extensively by Yip and co-workers to study the dynamics of grain-

boundary behavior and has proven valuable in uncovering and illustrating several grain-boundary processes.[19–22] Simulations have been conducted which demonstrate mechanisms of coupled sliding and migration of boundaries,[19] grain-boundary melting at temperatures below the bulk melting point,[20] and vacancy-migration paths in fcc and bcc boundaries.[21,22] Similar techniques have been applied by Mullins to study the propagation of matrix cracks,[23] and by Halicioglu to investigate the propagation of cracks in the stress field of microstructural obstacles.[24]

An element crucial to the success of molecular-dynamics simulations is the accuracy of the interatomic potentials describing the interactions between the atoms. Most of the early investigations used simple pairwise potentials. These simple potentials are now believed to be inadequate to describe many properties of metallic systems, structural irregularities, and the presence of chemically active impurities. The embedded-atom method (EAM) was developed by Daw and Baskes in order to remove these inadequacies from molecular-dynamics simulations.[25] This method, to be described later, has been used extensively by its originators to conduct investigations of properties and processes requiring an accurate treatment of chemical diversity and irregular structures. Daw and Baskes have computed the surface relaxations of Ni and Pd and computed adsorption energies for H onto several crystallographic planes.[25] These authors and their co-workers have also applied this method to the study of the interaction between H and moving cracks and dislocations.[26–28] Foiles has used the method to study surface segregation in a Ni-Cu binary alloy,[29] and has computed accurate liquid structure factors and phonon dispersion curves in a number of metals.[30,31] Recently, Baskes has applied the method to the investigation of grain-boundary fracture in Ni_3Al.[28]

In addition to the EAM, various investigators have put forth alternative descriptions of interatomic interactions which also overcome the inadequacies of simple pair potentials. Jacobsen, Nørskov, Puska, and Lang[32–34] have developed the effective-medium theory for interatomic interactions. In this approach, as with the EAM, the potential energy of an atom is related to the electron density in the region surrounding it. Unlike the EAM, the effective-medium theory is extended to express all numerical coefficients in terms of local electron density rather than allowing them to be fitted to experimental data. Finnis and Sinclair[35] have proposed a potential comprised of two-body repulsive interactions and an N-body attractive term which is also similar to the EAM. Unlike the EAM, however, the attractive term is described by a function written in terms of interatomic separation distance rather than local electron density. Ackland and Thetford[36] have improved the technique by adding a term to the repulsive potential which reflects core-core interactions at small interatomic separations. The improved potentials are better suited to MD calculations in which atoms may approach each other very closely.

In this investigation the techniques of molecular dynamics along with the embedded-atom method of Daw and Baskes[25] are combined in a study of the fundamental mechanisms of intergranular hydrogen embrittlement in Ni-Cr-Fe alloys. The EAM was selected above the effective-medium theory or the Finnis-Sinclair approach because it seemed to offer the best compromise between ease of impirical fitting and completeness of the physical description. This paper described the methodologies employed in the simulations, presents the major results of the investigation, and discusses the influence of the simulation technique on the results. The focus of the paper is on the verification and evaluation of the functions and the basic simulation technique itself. Although a proposed embrittlement mechanism is described in some detail, the emphasis of this paper is placed on the relation between aspects of the computational model and the simulated fracture scenarios. A complete presentation of the results, as well as their interpretation in terms of embrittlement mechanisms, will be given elsewhere.[37,38]

II. METHODOLOGY

The methodolgy employed in the investigation stems from the molecular-dynamics technique and the embedded-atom method of Daw and Baskes. Special techniques were used in order to simulate the behavior of materials under stress and temperature and to model the chemical properties of the target alloys. These methods are described below along with results of the testing procedure used to verify the model.

A. Basic concepts

The goal of the molecular-dynamics method is to describe the motion of individual atoms within a region of solid or liquid material. Equations of motion for each atom are solved simultaneously under the forces placed on each atom by its neighbors. Using the EAM, the interatomic forces are determined from the potential energy of the system,

$$E_s = \sum_{i=1}^{N} E_i = \sum_{i=1}^{N} F_i(\rho_i(\mathbf{r}_i)) + \tfrac{1}{2} \sum_{\substack{i,j \\ (i \neq j)}} \Phi_{ij}(r_{ij}) \ . \tag{1}$$

E_s is the potential energy of the solid relative to atoms at infinite separation, $\sum_i E_i$ is the average potential energy per atom, summed over all atoms i, F_i is the embedding energy of atom i (an attractive term), and Φ_{ij} is a repulsive pairwise potential between atoms i and j. ρ_i represents the total electron density that would exist at the location of atom i if that atom were to be removed. Following Daw and Baskes, the repulsive term is expressed as a screened Coulomb interaction,

$$\Phi(r_{ij}) = \frac{Z_i(\mathbf{r}_{ij}) Z_j(\mathbf{r}_{ij})}{r_{ij}} \ , \tag{2}$$

where the screened (effective) charge of each atom is written as an exponential decay in distance from the nucleus,

$$Z(r) = Z_0 e^{-\alpha r} \ . \tag{3}$$

Z_0 and α are tuning parameters used to fit the relation to

each species of atoms in the system. The electron density at the position of atom i is written as the sum over all neighboring atoms of their atomic electron density evaluated at that point,

$$\rho_i(\mathbf{r}_i)=\sum_{j\ (\neq i)}\rho_j^a(\mathbf{r}_i)\ . \tag{4}$$

The individual contributions from each atom, ρ_j^a, are written as a weighted sum of the free-atom electron densities for each atomic shell computed from Hartree-Fock theory. In the case of transition-metal atoms, only the s and d shells are considered,

$$\rho_j^a(\mathbf{r})=N_s\rho_j^s(\mathbf{r})+(N-N_s)\rho_j^d(\mathbf{r})\ . \tag{5}$$

N is the total number of outer-shell electrons for the atom and N_s is a tuning parameter (between 0 and N) used to fit the function to the behavior of each species in the system.

The embedding energy itself, $F_i(\rho)$, is obtained from Puska[39] in the case light elements or from Foiles's empirical treatment[29] in the case of heavier transition elements. In either case, the functions are determined independently without introducing additional adjustable parameters. As a result, the energy of the system may be expressed by determining values of N_s, Z_0, and α for each species to be included.

B. Function-fitting procedures

The goal of the function-fitting procedure within this investigation was to determine a set of EAM functions that can describe an alloy system consisting of Ni, Cr, Fe, and small quantities of H. Functional forms described above have been used and the adjustable parameters tuned to achieve agreement with various experimental quantities. Functions for Ni and H were obtained using the original scheme of Daw and Baskes. The functions for Cr and Fe were obtained using a new technique developed for the extraction of functions for an element, given data on a binary alloy in which it exists.

The first step in this process was to use the established Daw and Baskes method to fit the majority of the nickel parameters to pure-nickel data, then to fit additional nickel variables along with the hydrogen parameters to data from the Ni-H system. Following the procedure set forth by Daw and Baskes,[25] the values of Z_0 and α for Ni were obtained by matching computed and experimental values for the three cubic elastic constants and the phase-change enthalpy, $\Delta H_{\text{fcc-bcc}}$. The values were matched iteratively adjusting Z_0 and α at arbitrary N_s until the desired quantities were accurately calculated. As discussed by Smith,[37] the lattice constant and average energy per atom are "hardwired" into the embedding energy (i.e., judiciously selected and fixed) and are therefore always reproduced properly. For this reason, they are not used in the tuning process. After the Ni parameters were determined, N_s of Ni and α of H were fitted by simultaneously matching the heats of solution and migration of H in Ni. As with the first parameters, these fits were performed with an iterative search.[37]

Once the Ni and the H functions were established, parameters for Cr and Fe were fitted to experimental values for the Ni-Fe and Ni-Cr systems with use of our new technique. The objective of this procedure was to generate a set of functions for both Fe and Cr that would accurately represent their behavior in the Ni-rich alloys. Toward this end, the Cr and Fe parameters were adjusted so as to match experimental quantities of the fcc binary alloys to computed values for a model binary possessing the same composition. Since the Ni functions had already been fitted, only parameters for either the Cr or Fe functions were adjusted to fit the alloys.

Since a large number of iterations are required to fit each parameter, it is important to speed up the core of the calculation as much as possible. Toward this end, we developed a special method to describe the binary alloys in EAM formalism. Rather than construct computational cells containing two species of atoms, the alloy was represented as a collection of "effective" atoms, each prossessing a set of average functions computed from the individual functions of the species in the alloy. Using this method, it is possible to treat the alloy as a collection of identical atoms, which greatly speeds and simplifies the calculation of energies and elastic constants. Each of the functions required for the calculation of a monatomic solid were defined as weighted averages of the corresponding Ni functions and the Cr or Fe functions to be tuned; the atom fraction composition was used as the weighting factor. This method was used to tune the Cr and Fe parameters to experimental values of the phase-change enthalpy $\Delta H_{\text{fcc-bcc}}$ and the three elastic constants of the alloys. It must be noted that the effective atoms were only used in this stage of function fitting and were not employed in the verification procedures or in the final simulations.

In the effective-atom representation, the system is treated as a collection of identical atoms, each of which possesses the average properties of the individual species within the actual alloy. Expressions for the effective functions may be obtained from the average energy per atom, $\langle E\rangle$, averaged over the N atoms comprising the sample:

$$\begin{aligned}\langle E\rangle&=\frac{1}{N}\left[\sum_{i=1}^{N}F_i(\rho_i(\mathbf{r}_i))+\tfrac{1}{2}\sum_{\substack{i,j=1\\(i\neq j)}}^{N}\Phi(r_{ij})\right]\\&=\langle F_i(\rho)\rangle+\tfrac{1}{2}\left\langle\sum_{\substack{j=1\\(j\neq i)}}^{N}\Phi(r_{ij})\right\rangle\ .\end{aligned} \tag{6}$$

If it is assumed that the electron density, ρ_i, is fairly uniform from atom to atom, then $\langle F_i(\rho_i)\rangle$ may be written

$$\langle F_i(\rho)\rangle=X_{\text{Ni}}F_{\text{Ni}}(\langle\rho_i\rangle)+X_MF_M(\langle\rho_i\rangle)\ , \tag{7}$$

where $\langle\rho_i\rangle$ is the average of ρ_i for all atoms, X_{NI} is the atom fraction of Ni, and M represents the non-nickel species in the alloy (either Fe or Cr). Provided that the interatomic distances r_{ij} do not depend greatly on the individual species, $\langle\rho_i\rangle$ may be written

$$\langle\rho_i\rangle=\left\langle\sum_{j\ (\neq i)}\rho_j^a(r_{ij})\right\rangle=\sum_{j\ (\neq i)}\langle\rho_j^a(r_{ij})\rangle\ , \tag{8}$$

TABLE I. Best-fit tuning parameters for Ni, H, Cr, and Fe.

	N_s	Z_0	α
Nickel	0.6	28	1.92
Hydrogen	1.0	1	1.75
Chromium	0.4	24	1.70
Iron	0.8	26	1.79

where

$$\langle \rho_j^a(r) \rangle = X_{\mathrm{Ni}} \rho_{\mathrm{Ni}}^a(r) + X_M \rho_M^a(r) \ . \tag{9}$$

The repulsive term $\langle \sum_j \phi(r) \rangle$ is computed as the average repulsion of nickel atoms interacting with average neighbors, and M atoms interacting with average neighbors,

$$\left\langle \sum_{j\ (\neq i)} \phi_{ij}(r_{ij}) \right\rangle = \left[X_{\mathrm{Ni}} \sum_{j\ (\neq i)} \phi_{\mathrm{Ni}\text{-}n}(r_{ij}) + X_M \sum_{j\ (\neq i)} \phi_{M\text{-}n}(r_{ij}) \right] . \tag{10}$$

The interaction with a Ni atom and an average atom is written

$$\begin{aligned} \Phi_{\mathrm{Ni}\text{-}n}(r) &= X_{\mathrm{Ni}} \Phi_{\mathrm{Ni}\text{-}\mathrm{Ni}}(r) + X_M \Phi_{M\text{-}n}(r) \\ &= \frac{Z_{\mathrm{Ni}}(r)}{r} [X_{\mathrm{Ni}} Z_{\mathrm{Ni}}(r) + X_M Z_M(r)] \\ &= \frac{Z_{\mathrm{Ni}}(r)}{r} \langle Z(r) \rangle \ . \end{aligned} \tag{11}$$

With this development,

$$\begin{aligned} \left\langle \sum_{\substack{i,j \\ (i\neq j)}} \phi_{ij}(r) \right\rangle &= \sum_{\substack{i,j \\ (i\neq j)}} \frac{\langle Z(r) \rangle}{r} [X_{\mathrm{Ni}} Z_{\mathrm{Ni}}(r) + X_M Z_M(r)] \\ &= \sum_{\substack{i,j \\ (i\neq j)}} \frac{\langle Z_i(r) \rangle \langle Z_j(r) \rangle}{r_{ij}} \\ &= \sum_{\substack{i,j \\ (i\neq j)}} \langle \phi_{ij}(r) \rangle \ . \end{aligned} \tag{12}$$

TABLE II. Best-fit and experimental quantities used in the tuning process.

	Meas.	Calc.
Pure material		
Nickel		
Lattice constant (Å)	3.524[a]	3.524
Binding energy (eV/at.)	4.450[b]	4.450
Elastic constant (eV/Å^3) C_{11}	1.554[c]	1.477
C_{12}	0.955	0.952
C_{44}	0.729	0.774
H in nickel		
ΔE_{soln} [eV/(H atom)]	0.17[d]	0.173
ΔE_{mig} [eV/(H atom)]	0.41[e]	0.352

Binary systems

Ni-Cr (at. % Cr)	Lattice constant (Å) Meas.[f]	Lattice constant (Å) Calc.	Binding E (eV) Meas.[g]	Binding E (eV) Calc.	C_{11} Meas.[h]	C_{11} Calc.	C_{12} Meas.	C_{12} Calc.	C_{44} Meas.	C_{44} Calc.
10	3.535	3.535	4.425	4.426		1.488		0.967		0.781
20	3.547	3.547	4.395	4.396	1.543	1.500	0.959	0.982	0.802	0.787
30	3.562	3.561	4.357	4.362		1.504		0.993		0.787
40	3.580	3.567	4.315	4.323		1.502		1.001		0.785
50	3.599	3.593	4.267	4.282		1.496		1.006		0.780
Ni-Fe (at. % Fe)										
10	3.536	3.535	4.457	4.452	1.52	1.454	0.923	0.932	0.762	0.773
20	3.548	3.548	4.452	4.448	1.45	1.438	0.900	0.917	0.753	0.773
30	3.560	3.560	4.437	4.439	1.44	1.420	0.901	0.902	0.744	0.769
40	3.573	3.574	4.413	4.425	1.28	1.402	0.817	0.891	0.735	0.761
50	3.585	3.589	4.384	4.405	1.20	1.392	0.758	0.999	0.725	0.752

[a]Reference 42.
[b]Reference 43.
[c]Reference 44.
[d]Reference 45.
[e]Reference 46.
[f]References 47 and 48.
[g]Reference 49.
[h]References 50 and 51.

Inserting Eqs. (7)–(12) into Eq. (6) allows the average energy of the system to be simply expressed in terms of the prefitted nickel functions and the tuning parameters of the species to be fitted. The parameters are adjusted in order to achieve agreement with experimental data of the binary system. In this study, the parameters for Cr and Fe were selected in order to maximize agreement over a wide range of composition, X_{Ni}.

The results of the fitting procedure are summarized in Tables I and II. Table I lists the parameters ultimately selected for each of the functions for each element. Table II compares the experimental and best-fit values of all the quantities used in the tuning process.

C. Function-verification procedure

As described previously, the function-fitting operation was successful in tuning parameters to the various experimental quantities that could be incorporated into the fitting process. This is, however, insufficient to guarantee that the functions will perform adequately in actual molecular-dynamics simulations. With the exception of the hydrogen parameters, which were in fact fitted with complete minimization runs, all of the function fitting had been accomplished in terms of quantities calculated for a single atom in a perfect lattice. Elastic moduli were defined by the derivatives of E rather than by measuring a cell's response to stress. Defects and surfaces were ignored completely and the assumptions used in developing the average atom picture of the Ni-Cr and Ni-Fe binary alloys were not previously tested. Furthermore, the fitting process utilized no information at all about the ternary system Ni-Cr-Fe. In order to cover these points and verify that the functions would be suitable for use in molecular-dynamics simulations, a number of verification runs were performed using the static-minimization technique.[37] In order to verify the results of the tuning process, runs were made for pure nickel, Ni-H, and the binary and ternary metallic alloys.

Nickel functions were tested by performing minimizations to yield the valency-formation energy as well as an experimental measure of the bulk modulus. In addition, approximate surface-energy results were obtained from a preliminary investigation of grain boundaries in pure Ni. The major results of the verification procedure are presented in Table III, which shows that excellent agreement is achieved in each of these cases.

Verification of the hydrogen functions was accomplished by computing the binding energy of H to free Ni surfaces. As in the case of surface energies, the binding energy runs were performed on grain-boundary samples for which the surfaces do not possess a clear crystallographic orientation. As reported in Table III, values for the binding energy were within 20% of measured values.

Verification for the Cr and Fe functions was achieved by making minimization runs for several computational cells possessing various alloy chemistries. Ternary cells were prepared with a variety of [Cr]/[Fe] ratios for nickel concentrations between 60% and 100%. Average energies were computed and the deviation between these results and measured thermodynamic parameters was within 1% for all compositions. In addition, an Inconel Alloy 600 (Ni-16Cr-9Fe) cell was minimized to obtain values of energy and equilibrium lattice constant in excellent agreement with measured values.

TABLE III. Results of function-verification process.

Parameter	Calculated value	Standard value	Ref.
		Nickel	
Bulk modulus (GPa)	183	181	52
Vacancy-formation energy (eV)	1.34	1.4	53
Surface energy (eV)	0.1	0.11	54 55
		Hydrogen	
Binding energy to Ni surface (eV)	−2.5	−2.9	54 55
		Inconel Alloy 600	
Average energy per atom (eV)	4.413	4.407	56
Lattice constant (Å)	3.552	3.56	56

D. Simulation methodology

1. Sample preparation

Computational cells used in this investigation were prepared as coincident-site-lattice grain-boundary models with periodic borders in two directions. Periodicity was imposed in the grain-boundary plane and the nonperiodic direction (perpendicular to the boundary plane) was used as the tensile-stress axis as illustrated in Fig. 1. Typical cells contained between 325 and 500 atoms, with cell lengths in the periodic directions averaging 11 Å, and the overall length in the nonperiodic direction generally 40 Å from free surface to free surface.

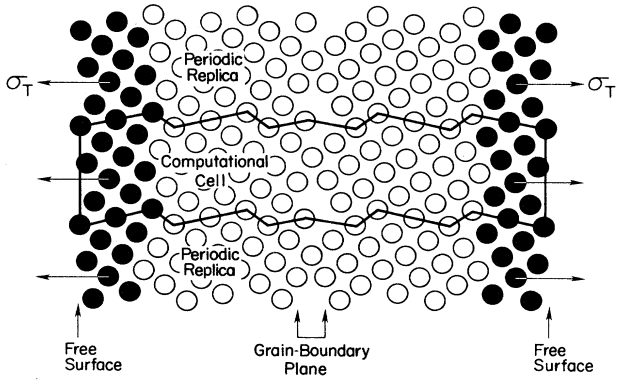

FIG. 1. Tensile stress applied to the nonperiodic direction of a computational cell. External force is applied to atoms (shaded) within about 5 Å of the free surfaces. Cells are periodic in two directions with periodic lengths averaging 11 Å, and the average overall cell length is 40 Å surface to surface.

Since many of the simulations were performed on alloy systems, important consideration had to be given to the assignment of a chemical identity to each atom. Because the alloys being addressed are known to be random, the assignment was made in order to achieve a desired overall chemical composition as well as to assure that no erroneous short-term ordering had been imposed. The actual assignments were obtained from an iterative "trial-and-error" procedure. Each atom in the cell was randomly assigned an identity using probabilities taken from the bulk composition of the alloy. The cell was then checked for any erroneous short-term ordering, and if the cell did not appear sufficiently random the procedure was repeated.[37]

Before subjecting the computational cells to simulations under stress and temperature, each starting structure was "minimized" into a low-energy (0-K) configuration. This step was used to remove any extraneous configurational energy present in the initial structure.

2. *Simulations*

Simulations were performed by subjecting the cells to dynamic simulations under stress and temperature. In each of the simulations, the periodic lengths of the cells were held fixed throughout the run. Cells were brought to the target temperatures through an equilibration process in which kinetic energy is added or subtracted from atoms uniformly across the cell. The temperature-equilibration model operates on an energy deficit and/or excess expressed in terms of the difference between the target and the actual temperature.[40] Once the temperature-equilibration period is over, forces are slowly applied to the atoms near the surface of the cell and increased linearly in time. The forces were increased until the cell fractured, usually within 10 000 time steps of length 2 fs. The force ramp rate was set to 2.7×10^{-4} eV/Å^3 as suggested by Daw in order to minimize the effect of elastic waves on the results.[41]

E. Verification of simulation methodology

Before performing grain-boundary simulations, several runs were made in order to verify the basic procedure and the use of the EAM functions in a dynamic simulation. Simulations were made for blocks of perfect crystal with compositions representative of pure Ni, Inconel Alloy 600, and Inconel Alloy 690. Runs were conducted with the application of temperature and external stress in order to verify the following.

That the temperature-equilibration model performs properly, both in bringing atoms to the correct thermal velocities and in properly transferring kinetic energy into thermal expansion.

That the applied force and measured stress are in agreement, the time- and force-step increments are properly selected, and the stress-strain curves reflect a reasonable effect of temperature and of alloy chemistry.

The temperature-equilibration and thermal-expansion behavior were investigated by running several cells at various temperatures in the absence of an applied load. The cell temperature was initialized to 20 K, and the simulation extended to about 1000 time steps of length 2 fs in order to bring the cell up to the specified target temperature. The temperature-versus-time curve takes the form of an exponential decay as expected from the formulation of the model, and it was determined that a 1000-step equilibration time would be adequate for all target temperatures up to about 620 K. The results of these runs were also used to verify that the cell heating was being properly communicated into thermal expansion. As shown in Table IV, expansion coefficients are in reasonable agreement with experimental values. While agreement on the nickel values is quite good, expansion coefficients for both Inconel Alloy 600 and Inconel Alloy 690 were overpredicted by as much as 35% and 21%, respectively. Since thermal expansion results from an asymmetry in the potential energy of an atom around the equilibrium separation distance, an overprediction of the expansion coefficient suggests that either the repulsive portion of the curve is too steep or that the attractive portion is not steep enough. The fact that the error is reduced in moving from Inconel Alloy 600 to Inconel Alloy 690 (increased Cr at constant Fe) suggests that some error exists in the shape of both the Cr and Fe functions, but that the errors are in opposite directions.

TABLE IV. Computed and experimental thermal-expansion coefficients.

Material	α [$10^{-6}(\Delta l/l)$/K] Calc.	Meas.	Ref.
Ni	13	13	57
Inconel Alloy 600	19	11–14	58
Inconel Alloy 690	17	14	59

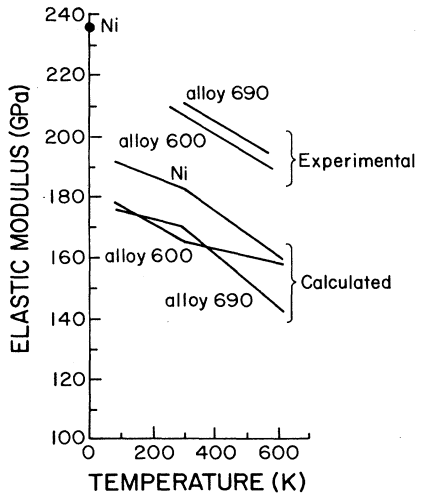

FIG. 2. Experimental and computed temperature dependencies of elastic moduli of Ni, Inconel Alloy 600, and Inconel Alloy 690. The upper two curves are the experimentally determined Young's moduli for polycrystalline Inconel Alloys 600 and 690. The single data point marked Ni at the top of the plot represents the value of C_{11} for Ni used in the fitting. The lower curves represent the elastic moduli of the computational cells of Ni, Inconel Alloy 600, and Inconel Alloy 690 as discussed in the text.

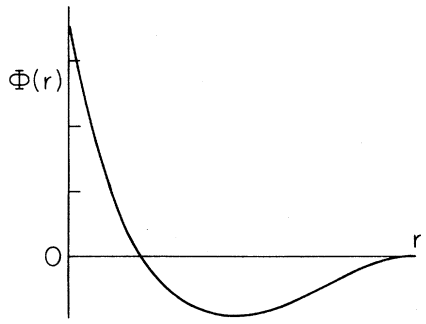

FIG. 3. Radial dependence of the interatomic potential.

Stress-strain simulations were conducted for each of the alloys at temperatures of 77, 300, and 620 K. Young's modulus was determined in each case and compared to the measured values. As shown in Fig. 2, the computed moduli possess the correct temperature dependence, although the absolute magnitudes are rather low. The apparent discrepancy is explained by the fact that the overall strains used in determining the computed moduli were on the order of 10%, vastly greater than the elastic limit of real material. Since the elastic modulus measures the change in stress (or force) per unit strain, the modulus can be related to the curvature of the potential-energy–versus–atomic-separation plot illustrated in Fig. 3 [$dF/dR = d(dE/dR)/dR = d^2E/dR^2$]. As the material is strained in tension, the separation between atoms increases and, as is evident from Fig. 3, the curvature of the function decreases. The result is that the measured modulus decreases with increasing strain and the average value measured over a strain of 0–10% will be significantly less than the value measured over a range from 0.0% to 0.5%, very near the bottom of the well. Computed values of the modulus could not be obtained for a more realistic strain range because thermal fluctuations preclude accurate measurement of stress or strain in this regime.

Additional runs for which the force rate was halved at constant time-step length, and the time-step length was halved at constant force rate, were made for the Inconel Alloy 600 sample at 300 K. These runs were used to check that force rate and step sizes had been properly selected. In each case the resulting value of the Young's modulus for the cell was used for comparison and found to be insensitive to the values selected for either parameter. Values of the modulus changed by only 3 GPa when the step length and force rate were modified. The insensitivity confirms that the values are reasonable.

A final check was made by comparing the stress measured at the center of the cell to the stress computed by dividing the applied force presented at the free surfaces by the cross-sectional area of the cell. The fact that these values were in proper agreement confirms that both the time-step length and force ramp rate were properly chosen. As described by Smith,[37] a significant disagreement in the stress values would suggest that the sample was being stressed too quickly and that elastic waves were not being given sufficient time to communicate the stress evenly throughout the cell.

TABLE V. Test matrix of selected runs. ×'s indicate simulations to be run both with and without hydrogen. GB no. refers to grain-boundary configurations described in Fig. 4.

GB no.	Temperature (K) 77	188	300	620
		Nickel		
1	×			
2				
3				
4				
5	×		×	
6				
		Inconel Alloy 600		
1	×		×	×
2	×		×	×
3			×	
4	×	×	×	×
5	×	×	×	×
6			×	
		Inconel Alloy 690		
1			×	×
2				
3				
4				
5			×	×
6				

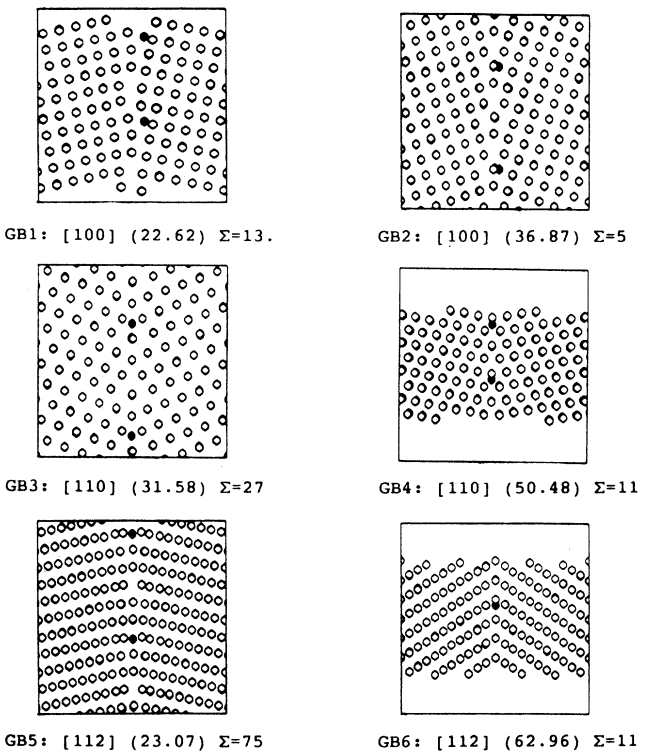

FIG. 4. Grain-boundary configurations selected for study. In each case the rotation axis is out of the page. Dark atoms represent H sites. Values written below each boundary reflect the rotation axis (angle) and Σ value, reflecting the inverse of the fraction of lattice sites coincident to each lattice.

III. TEST MATRIX

The collection of simulations performed within this investigation is designed to measure the influence of H on grain-boundary fracture and to determine how this influence is affected by variations in grain-boundary structure, temperature, and chemistry. The influence of H is measured in terms of changes in the stress-strain–to–fracture curve of the sample and in the time evolution of the grain-boundary geometry. The independent variables have been chosen to reflect the controls one would have in a typical laboratory experiment. Selected values of the independent variables are outlined in the test matrix of Table V, and were chosen in order to best approximate the conditions found in experimental studies and to sample a wide range of each variable. When cells were hydrogenated, a single H atom was placed along the boundary, bringing the local H concentration in the plane to about 10 at.%. The grain-boundary configurations selected for study are shown in Fig. 4.

TABLE VI. Overview of hydrogen embrittlement results.

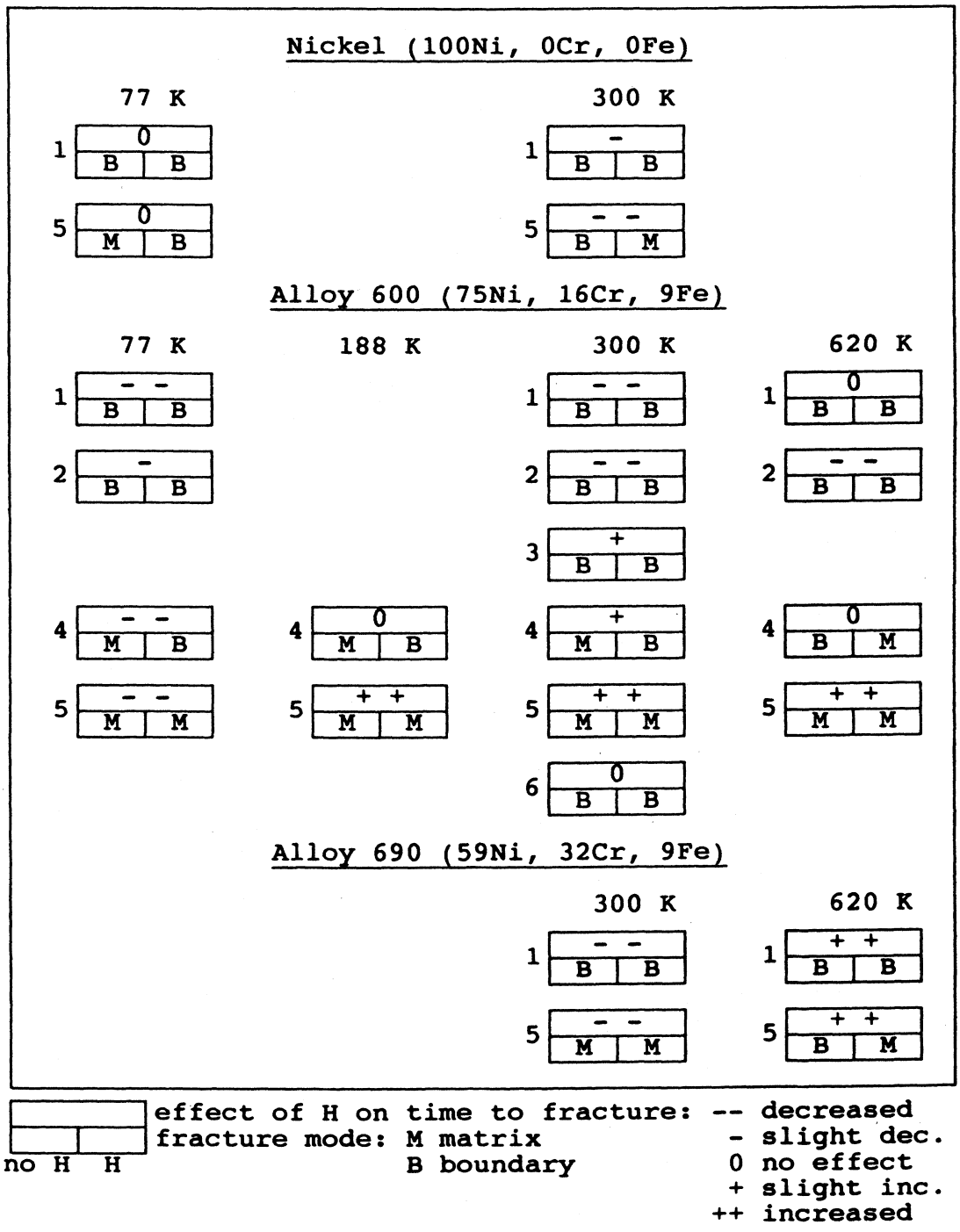

IV. RESULTS

Each of the boundary cells selected for study was prepared in the proper composition and brought into a minimum-energy configuration via static minimization. The cells were then run through tensile test simulations with fixed periodic borders. Results for each run listed in Table V are summarized in Table VI, which presents the fracture mode observed in each case along with the overall effect of H on the time to failure of each cell.

As noted in the legend of Table VI, entries in the top portion of each cell describe the effect of H on the time to fracture of each cell as compared to the nonhydrogenated case. Entries of $--$, $-$, 0, $+$, and $++$ indicate a range of effects from a significant reduction in lifetime to a significant enhancement, respectively. Changes in lifetime of more that about 5% were considered significant. Null (0) values are recorded when the extension-versus-time curves for hydrogenated and nonhydrogenated samples could not be resolved within the high-frequency noise existing in each curve. Entries in the lower portions of each cell indicate the fracture mode observed for the nonhydrogenated case on the left and the hydrogenated case on the right. An entry of *B* indicates that the cell broke apart within a few atom distances of the boundary plane; an entry of *M* indicates that the cell fractured within the matrix region between the boundary and the surface.

As noted previously, each of the results of this investigation have been reported and discussed in detail in other publications.[37,38] These papers focus on interpreting the results in terms of embrittlement mechanisms. In this paper attention is turned to the influence of simulation methodology on the results in order to better understand how the model behaves. Although the embrittlement mechanism is reviewed, the emphasis of this section is placed on the relation between aspects of the computational model and the simulated fracture scenarios.

A. Boundary fracture with H and without H: (*B*,*B*)

In the cases for which fracture occurs consistently at the boundary, the hydrogenated and nonhydrogenated samples generally behave similarly until the point of fracture. In nearly all cases observed, the strain curves of the samples are nearly identical, separating only as one of the samples fractures at the boundary. Typical strain curves illustrating this behavior are displayed in Fig. 5. The evolution of the atomistic configuration is also similar from case to case throughout the fracture process. Under the influence of external stress the samples elongate uniformly in the matrix region with a slightly different strain rate at the boundary plane. As strain across the boundary is increased, the restoring force is reduced and the boundary separates rapidly. Depending upon the atomistic configuration of the first few boundary planes, the separation may happen in either a clean brittle fashion or one in which bands of material are drawn into the center from either side.

A unique case in this class is the result of the GB-1 run at 620 K. The hydrogenated sample appears to undergo a grain-boundary migration in which the initial gap is

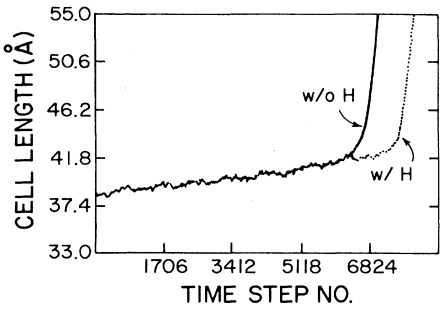

FIG. 5. Typical stress-strain curve for GB-1 Inconel Alloy 690 (620 K).

closed and several atoms transferred across the boundary plane. The resulting configuration, just prior to fracture, is shown in Fig. 6.

The large number of cases that exhibited failure at the boundary both with H and without H make it possible to compare the effects of several control variables on the process of boundary fracture. Specifically, the effects of boundary structure, temperature, and alloy chemistry may be addressed as is done in Refs. 37 and 38. In this paper, only the effect of structure is reviewed.

From Table VI, it is seen that the effect of structure may be analyzed by comparing the runs of GB-1, GB-2, GB-3, and GB-6 in Inconel Alloy 600 at 300 K. In the first two cases, the H sample failed measurably sooner than its nonhydrogenated counterpart. In GB-3, H appears to increase the time to failure by a small amount, and in GB-6 there is no measureable effect. Interestingly, the boundaries for which H appears to reduce lifetime each process tunnels of open area when viewed along the rotation axis (Fig. 4), while the unaffected boundaries do not. An additional comparison can be drawn by consid-

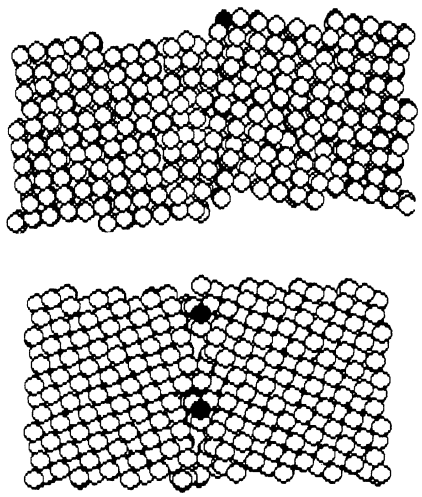

FIG. 6. Comparison of structures developed in GB-1 and GB-2 at 620 K. (a) GB-1 after the initial transfer of material across the boundary has eliminated the channels and altered the structure. (b) GB-2 possessing its original channels.

ering the results of GB-1 and GB-2 for Inconel Alloy 600 at 77 and 620 K. At the low temperature, the reduction in time to failure due to H is decreased in both cases relative to the 300-K values, but the reduction is greater for GB-2. At the high temperature, the hydrogenated sample of GB-2 exhibits a significant reduction in time to failure, while there is virtually no effect of H on the time to failure of GB-1. The comparison between GB-1 and GB-2 at high temperature appears to reveal a trend similar to the comparison performed at 300 K. While the high-temperature case of GB-1 experiences a large amount of restructuring at the boundary, GB-2 did not. As a result, it is expected that open holes which persisted in GB-2 to high temperature were removed in GB-1. These data suggest that a reduction in time to fracture may be correlated to the presence of low-density areas or open channels at the boundary.

B. Boundary fracture with H and matrix fracture without H: (M,B)

Cases in which the nonhydrogenated sample exhibited fracture in the matrix while the hydrogenated sample fractured along the boundary include GB-4 in Inconel Alloy 600 at 77, 188, and 300 K, and GB-5 in nickel at 77 K.

In GB-4, the matrix fracture which is observed in the absence of H is a process involving a large amount of deformation spread over an area of several lattice constants. As illustrated in Fig. 7(a), highly deformed areas occur in the material midway between the boundary and surfaces on either side. Eventually, failure occurs in one of these

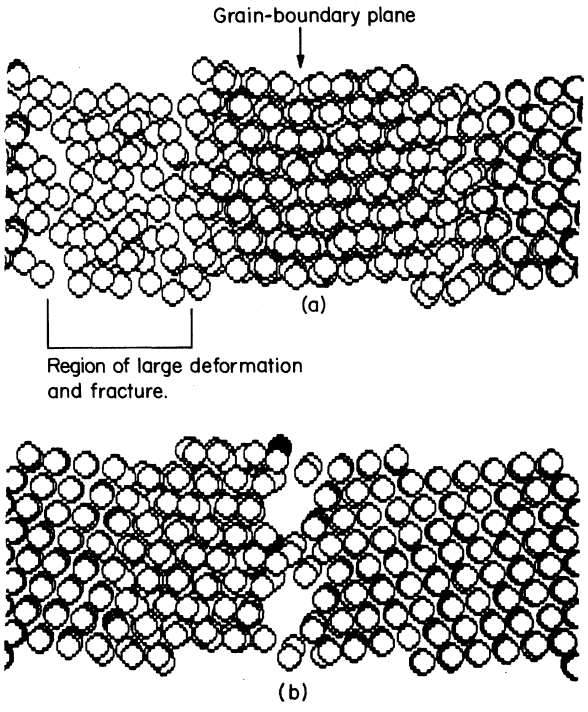

FIG. 7. Post-fracture configurations for GB-4 of Inconel Alloy 600 at 77 K. (a) Nonhydrogenated, (b) hydrogenated.

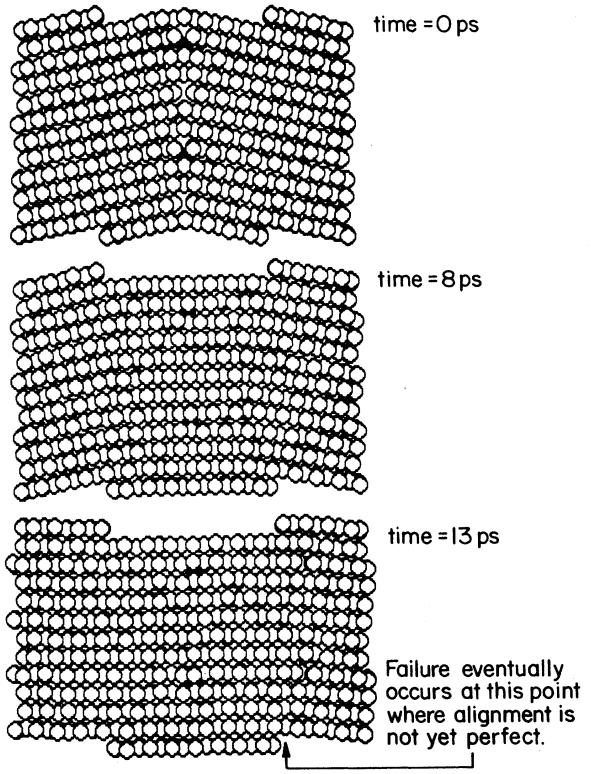

FIG. 8. Elimination of grain-boundary mismatch in GB-5 of Inconel Alloy 600 at 77 K.

regions. In the hydrogenated cases at temperatures of 77, 188, and 300 K, the deformation seems to extend over a wider region of material up to the boundary plane. In each of these cases fracture occurs in the boundary and the hydrogen atoms become bound to one of the surfaces as shown in Fig. 7(b). The strain curves reveal that the presence of H reduced the time to failure at 77 K, had no effect at 188 K, and mildly increased lifetime at 300 K. In the 300-K case it appears that the increased lifetime results from the fact that the area of deformation is more uniformly distributed in the H sample. As such, it takes a few time steps longer for a sufficient amount of strain to cause fracture to develop in any local region.

Before closing this subsection it is important to note several interesting cases of GB-5. As shown in Table VI, this sample generally failed away from the boundary in both the hydrogenated and nonhydrogenated cases. Each time, the grain boundary underwent a transformation in which the boundary-mismatch angle was eliminated under the influence of stress and temperature as illustrated in Fig. 8. As discussed in the next section, the elimination of boundary mismatch may be an artifact of the fixed periodic borders used in the model.

C. Reproducibility

Results of reproducibility tests conducted by rerunning GB-4 at 300 K reveal that the random selection of initial velocities used to achieve a desired temperature can have a measurable effect on the simulation results. Although

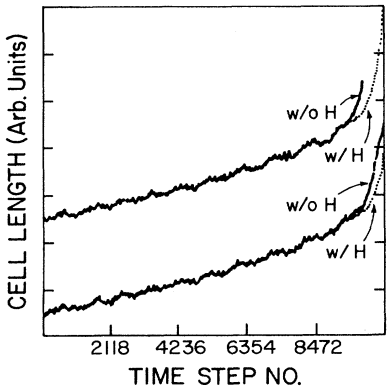

FIG. 9. Results of reproducibility runs. The upper set of curves comes from the first set of runs for GB-4 of Inconel Alloy 600 at 300 K. The lower set comes from the second set of runs for this case. In each set, the dark line is for the nonhydrogenated sample and the light line is for the hydrogenated sample.

fracture mode was unaffected, the time to failure is subject to variation. As illustrated by the curves of Fig. 9, the variation in time to failure for both hydrogenated and nonhydrogenated samples may be comparable to the difference in time to failure between the two samples. Under these circumstances the apparent influence of H on time to failure is dependent upon the chance selection of individual runs.

Physically, the variation in the strain curves is caused by a superposition of the random thermal motion of each atom onto its motion due to strain. Since the time to failure changed while the mode of fracture did not, the reproducibility results indicate that the basic mechanism of fracture is *not* influenced by the superposition, but that the speed with which it proceeds is affected. Inspection of the fracture configurations shows that failure is limited to a region containing only tens of atoms, confirming that a significant statistical effect is reasonable.

Results of these runs suggests that fracture mode is a more significant measure of embrittlement than is time to failure, and that changes in time to failure should be used only when they are large ($>10\%$) and only for a qualitative comparison.

V. DISCUSSION

A. General observations on fracture mechanisms and the evolution of cells

The post-fracture configurations presented in the previous section reveal two basic types of fracture. The first is a brittle fracture in which the sample separates in the grain-boundary plane as shown in Fig. 6(b). In this case the structure of the cell is largely unaffected except in the area within a few atomic distances from the boundary where appreciable changes in configuration may occur. Brittle fracture occurs on the grain-boundary plane in cases such as GB-1, GB-2, GB-3, and GB-6 for which the boundary is considerably weaker than the matrix material. The second type of failure is illustrated in Fig. 7(a) and occurs as a uniform deterioration in the lattice over a wide region of the sample following considerable elastic strain. The region which fails elongates uniformly until the combined effects of strain and thermal motion cause the atoms in the region to separate from one another. The second form of failure is observed both in the boundary and in the matrix region and occurs when the strengths of the boundary and matrix are comparable. Although these two processes appear different, they are similar in the respect that each occurs as a separation of the lattice planes which are perpendicular to the tensile axis, and the separation of material is fairly uniform along the directions perpendicular to the axis. Events in which small cracks nucleate at isolated points and then propagate through the material are not observed. Processes involving slip are also rare.

In assessing the fracture characteristics, it is important to consider the degree to which the observed behavior is controlled by the methods used in the simulations. As discussed in the following paragraphs, the use of periodic border conditions with fixed lengths is expected to have a significant influence on the results. Periodicity of the cell prevents the development of long-range spatial gradients in either stress or strain along the directions perpendicular to the stress axis. This restriction inhibits the propagation of cracks and promotes a fracture which is more uniformly distributed along the cross section of the cell. The use of static borders also promotes the fracture modes observed above by preventing the material from contracting along the directions perpendicular to the stress axis. As a result of these restrictions, the bulk of all atomic motion is directed along the stress axis during failure. For this reason it is expected that the nucleation and propagation of grain-boundary cracks as well as any effect of H on these processes is poorly treated by this model.

An observation which is largely attributable to the configuration of the computation cells is the reorientation of lattice planes observed in GB-5. As shown for a specific case in Fig. 8, a symmetric alignment develops as atoms near the center of the cell move collectively in a direction perpendicular to the boundary. As the atoms move, the grain-boundary plane containing the lattice mismatch separates into two planes which travel toward the opposite surfaces. It is important to note that the motion of these planes occurs without any associated slip or structural transformation. The $(11\bar{1})$ planes on either side of the mismatch planes appear continuous and merely to be bent through a small angle at the mismatch plane. Although the basic process displayed by this cell is realistic (lattice planes may certainly rotate under the influence of stress) the specific manner in which it proceeds as well as its overall effect of the grain boundary are undoubtedly artifacts of the periodic borders and narrow cell size. The transformation displayed in Fig. 8 takes place as atoms move in a direction exactly perpendicular to the nonperiodic direction, and begins at the center of the cell moving outward. While it is not clear that additional border conditions would restrict this transformation, in an actual boundary, deviations from

periodicity will tend to impede the collective motion required for the transformation, and additional microstructural elements may exert forces retarding the motion of the boundary plane.

A second interesting process occurs in the case of GB-1 of Inconel Alloy 600 at 620 K, in which the boundary appears to exhibit the first steps of migration prior to fracture (Fig. 6). In this case it is recalled that thermal motion of the atoms in the boundary region closed gaps which had originally been present in the boundary plane. Atoms which entered the gaps were preferentially transferred from one crystal to the other, causing a migration of the boundary plane. It is though that this event results largely from the periodic nature of the sample and would not be expected to occur frequently in actual grain boundaries. In a more realistic boundary configuration, deviations from periodicity would be expected to disrupt the transfer of atoms across the boundary plane at several points and thereby impede its migration. In contrast, the initial closing of the boundary gap by the thermal motion of individual atoms is a process which is not directly dependent on periodic borders or the proximity of the boundary to a free surface. Local changes in structure promoted by these events appears to be realistic behavior for a true material.

B. Correlations between fracture and grain-boundary structure

Having discussed the basic behavior of the cells, the next step is to focus attention on the correlation between the dependent variables used to measure embrittlement (mode and time to failure) and the independent variables controlled in the study (chemistry, structure, and temperature). Each of these topics is covered at length in Refs. 37 and 38. In this paper, only the link between embrittlement and structure is reviewed.

In the fracture category (B,B), in which both hydrogenated and nonhydrogenated samples fail at the boundary, a correlation between embrittlement and boundary structure is suggested by the fact that at 300 K, the time to failure of GB-1 and GB-2 in alloy 600 was measurably reduced by H, but was unaffected in the cases of GB-3 and GB-6. This correlation is illustrated in Table VII(a) along with additional information obtained at 77 and 620 K. Although results only exist for one run of each of these samples, it is noted that the changes in time to fracture in GB-1 and GB-2 are larger than the changes discussed in the reproducibility section, and that the strain curves of GB-6 are almost identical in the hydrogenated and nonhydrogenated case. The selection of two identical runs from a distribution of possible results seems unlikely unless the range of behavior is reasonably small and therefore adequately represented by the available results.

The variable which correlates most strongly to embrittlement is the existence of low-density areas at the boundary. At 300 K, the correlation between reduced time to failure and open channels is supported by the starting structures of Fig. 4 and by the time-dependent evolution of each boundary. As explained earlier, GB-1 and GB-2 possess open channels and were each embrittled while GB-3 and GB-6, which do not possess open areas, were not embrittled. At 77 K, thermal motion does little to

TABLE VII. Structure correlations for (a) fracture group (B,B) and (b) for groups (M,B) and (M,M). The symbols $--$, $-$, $++$, and 0, have the same meaning as in Table VI.

(a) Group (B,B)

GB	Axis	Δt	structure
		Inconel Alloy 600 at 300 K	
1	[100]	$--$	open channels
2	[100]	$--$	open channels
3	[110]	$+$	no channels
6	[112]	0	no channels
		Inconel Alloy 600 at 77 K	
1	[100]	$--$	large channels
2	[100]	$-$	small channels
		Inconel Alloy 600 at 620 K	
1	[100]	0	channels removed
2	[100]	$--$	channels preserved

(b) Groups (M,B) and (M,M)

Fracture mode	Structure
	GB-4 in Inconel Alloy 600 at 77, 188, and 300 K
(M,B)	significant mismatch between planes at grain boundary
	GB-5 in Inconel Alloy 600 at all temperatures
(M,M)	mismatch removed due to transformation process at the boundary

alter the boundary configuration and as a result, the channels of both GB-1 and GB-2 are preserved throughout the runs. It is evident from Fig. 4 that the channels of GB-1 are larger and more elongated than those of GB-2, and at 77 K, GB-1 is significantly embrittled while GB-2 is not. At 620 K, time-to-failure results of GB-1 and GB-2 are reversed with GB-2 becoming embrittled while GB-1 does not. At this temperature, thermal motion of the atoms tends to close the gaps in both cases, but as is shown in Fig. 6, while the basic structure of GB-2 is unaltered, GB-1 undergoes a grain-boundary–migration phenomenon in the hydrogenated sample which destroys the structure of the channels. The removal of the channels correlates with the reduction in susceptibility to H embrittlement.

An additional correlation between H embrittlement and boundary structure is suggested from the comparison of GB-4 results to those of GB-5. As shown in Table VII(b), in each of these cases the nonhydrogenated samples tend to fail away from the boundary, indicating that boundary- and matrix-region strengths are comparable. In the hydrogenated cases, however, GB-4 is often seen to fail at the boundary, while GB-5 consistently fails in the matrix. Inspection of boundary structure reveals that although GB-4 possesses no low-density areas it is an interface at which lattice planes meet with a finite mismatch angle. Structures of GB-5, on the other hand, tend to undergo realignment so that by the time fracture is reached the $(11\bar{1})$ planes meeting at the boundary do so with almost no mismatch angle. This comparison is consistent with the idea that hydrogen acts to weaken metal-metal bonds, but only does so significantly in areas of geometric irregularity.

C. Mechanisms of embrittlement

The correlations discussed above indicate that the active mechanism of hydrogen embrittlement in these samples is a weakening of metal-metal bonds caused by the presence of H. When present at grain boundaries that are intrinsically weak the influence of H is most significant in regions of grain boundary which possess open channels (as in GB-1 and GB-2), and when present at boundaries which are strong relative to the matrix the influence of H is most pronounced at an irregularity in lattice structure (as in GB-4). The results indicate that the influence of H on a given metal-metal bond depends upon the specific environment (density and arrangement) of the atoms in the immediate region. Specifically it is suggested that H exerts its strongest influence in areas of high geometric asymmetry which cause large asymmetries in the potential wells of the atoms. The introduction of a perturbation (due to a new atom) into this type of region is more likely to have a deleterious effect on a critical bond than it would in an area in which the wells were symmetric and all similar to each other. In the first instance, a small perturbation could act to destabilize a bond which was only slightly stable originally. In the second case the bonds are uniform in both strength and direction and the effect of a small perturbation would be minimized by the dissipation of excess energy equally among all of the neighboring atoms.

Although the proposed mechanism appears sound, it is important to realize that its validity is based on the assumption that H perturbs the strength of both strong and weak bonds by roughly the same amount. If it were determined that the effect of H diminished to zero as the bond strength decreased, then the mechanism would not be viable. In order to investigate the validity of the proposed model, the effect of H on metal-metal bonds may be analyzed through a technique provided by Daw.[26] Using the EAM formalism, Daw has expressed the change in restoring force between two metal atoms due to the presence of an H atom as

$$\Delta f = F_m'' \rho_h \rho'(R_{mm}) , \tag{13}$$

where Δf is the change in force, ρ_h is the electron density contributed by the H atom, ρ' is the derivative of the electron density contributed by a metal atom with respect to the metal-metal separation distance, R_{mm}, and F_m'' is the curvature of the metal embedding energy with respect to the host-electron density, $d^2F/d\rho^2$.

In the case of a strong bond, the *M-M* separation distance is near the equilibrium value and, as such, ρ' and F_m'' are also at near-equilibrium values. In a weak bond, R_{mm} is greatly extended, reducing both ρ and ρ'. However, as ρ decreases, $F_m''(\rho)$ increases significantly. As a result, the magnitude of Δf may either increase or decrease in moving from strong to weak bonds, depending upon the relative changes in ρ' and F''. Since $\rho(r)$ is roughly linear, for R_{mm} values near or exceeding the equilibrium separation distance, ρ' does not vary much between strong and weak bonds and it may be safely assumed that the magnitude of Δf is comparable in each case. Since the perturbation in bond strength due to H does not diminish as the bond strength is reduced, the embrittlement mechanism may be viable.

At this point it must be noted that while the EAM can be used to detect the basic operation of a mechanism such as the one proposed, it is not the appropriate method to use in a detailed analysis of the mechanism. The inability of the model to explicitly account for changes in electron density caused by changes in the location of potential centers precludes an accurate calculation of energies and forces for detailed arrangements of atoms. Calculations along these lines must be done with more detailed quantum-chemical methods.

D. Significance of processes not modeled

In review of the simulation results and embrittlement mechanisms proposed it is important to consider the limited extent of the processes which have been modeled. Recall that the computational cells consist of single, isolated, periodic boundaries placed within 20 Å of a free surface on either side and loaded in pure tension along a direction perpendicular to the boundary plane. Periodic borders retard the operation of plastic processes, limiting fracture mechanisms to those which operate without slip and without the propagation of cracks. Significant elements missing from the model are the presence of defects

along the grain boundary and the presence of dislocations either generated within the boundary or incident from the matrix material.

The effect of the missing elements may be to cause the actual material to fail by mechanisms that occur well before the processes that have been modeled are activated. The observations of truly intergranular fracture in the absence of plastic flow in both Ni (Refs. 3 and 4) and Inconel 600 (Ref. 2) indicate that the mechanisms modeled may operate with reasonable frequency, but in order to gain a more complete picture of the effects of H its influence on dislocation processes must also be studied. Since any material will fail by the first failure mechanism to become activated, each of the competing processes must be understood.

VI. SUMMARY

EAM functions have been constructed for H, Ni, Cr, and Fe, and verified against several experimental quantities of Ni, Ni-H, and the Ni-Cr-Fe systems. Functions for Cr and Fe were obtained using a new technique by which functions may be extracted from experimental data of a binary system. The method has proven to be very fast and generates accurate functions. Lattice constant, elastic constants, surface energy, vacancy-formation energy, and average energy per atom are all accurately computed for pure Ni. Heats of solution and migration are accurately computed for H in Ni, and the composition-dependent values of lattice constant, elastic constants, and average energy per atom are accurately computed for Ni-Cr and Ni-Fe binaries. Thermal-expansion coefficients and the temperature dependence of Young's modulus were computed for nickel, Inconel Alloy 600, and Inconel Alloy 690, and found to be in agreement with the measured values for each material.

Dynamic simulations have been applied to six grain-boundary types in Ni, Inconel Alloy 600, and Inconel Alloy 690 at temperatures ranging from 77 to 620 K in order to evaluate the influence of H on the fracture behavior of the boundaries.

A significant correlation is found between hydrogen embrittlement and the presence of open channels along the boundary. An explanation for the correlation is proposed in which H acts more effectively to destabilize metal-metal bonds in areas where some of the bonds were already partially unstable, versus areas of perfect crystal where the potential wells of the atoms are more symmetrical and uniform.

The use of fixed-length, periodic border conditions appears to impede the operation of slip processes and the development of small, localized cracks. As such, the present model is better suited to the simulation of uniform decohesion across grain boundaries than to the simulation of crack propagation. The absence of dislocations from the model precludes the operation of many potential fracture mechanisms and restricts the model to the simulation of H embrittlement mechanisms which act in the boundary without plastic deformation.

ACKNOWLEDGMENTS

The authors gratefully acknowledge the Computer Aided Engineering Network at the College of Engineering, University of Michigan (Ann Arbor). Special thanks are due to Mike Baskes at Sandia National Laboratory for his many helpful discussions on the embedded-atom method. This work was funded by the Office of Basic Energy Sciences of the United States Department of Energy, under Contract No. DE-FG02-85ER45184.

---

*Present address: C-TAD Systems, Inc., 900 Victors Way, Ann Arbor, MI 48108.

[1]T. Boniszewski and G. C. Smith, Acta Metall. **11**, 165 (1963).
[2]M. Cornet, C. Bertrand, and M. Da. Cunha Belo, Metall. Trans. **13A**, 141 (1982).
[3]A. H. Windle and G. A. Smith, Met. Sci. J. **4**, 136 (1970).
[4]R. M. Latanision and H. Opperhauser, Jr., Metall. Trans. **5**, 483 (1974).
[5]H. K. Birnbaum, in *Electronic Structure and Properties of Hydrogen in Metals* (Plenum, New York, 1982).
[6]D. H. Lassila and H. K. Birnbaum, Acta Metall. **34**, 1237 (1986).
[7]T. Tabata and H. K. Birnbaum, Scr. Metall. **17**, 947 (1983).
[8]T. Tabata and H. K. Birnbaum, Scr. Metall. **18**, 231 (1984).
[9]M. Haigiwara and J. Chene, Scr. Metall. **18**, 877 (1984).
[10]B. B. Rath and I. M. Robertson, Metall. Trans. **2**, 2972 (1971).
[11]A. Roy, U. Erb, and H. Gleiter, Acta Metall. **30**, 1847 (1982).
[12]T. Watanebe, Res. Mechanica **11**, 47 (1984).
[13]C. L. Briant and R. P. Messmer, Philos. Mag. **42**, 569 (1980).
[14]C. L. Briant and R. P. Messmer, Acta Metall. **30**, 1811 (1982).
[15]C. L. Briant and R. P. Messmer, Acta Metall. **32**, 2043 (1984).
[16]M. E. Eberhart, K. H. Johnson, R. P. Messmer, and C. L. Briant, *Electronic Structure and Properties of Hydrogen in Metals* (Plenum, New York, 1982).
[17]R. P. Messmer and C. L. Briant, Acta Metall. **30**, 457 (1982).
[18]K. H. Johnson, Adv. Quantum. Chem. **7**, 143 (1973).
[19]R. Najafabadi and S. Yip, Scr. Metall. **18**, 159 (1984).
[20]F. Carrion, G. Kalonji, and S. Yip, Metall. **17**, 915 (1983).
[21]S. Yip, Comments Solid State Phys. **11**, 125 (1984).
[22]T. Kwok, P. S. Ho, and S. Yip, Surf. Sci. **144**, 44 (1984).
[23]M. Mullins, Scr. Metall. **16**, 663 (1982).
[24]T. Halicioglu and D. M. Cooper, Mater. Sci. Eng. **79**, 157 (1986).
[25]M. S. Daw and M. I. Baskes, Phys. Rev. B **29**, 6443 (1984).
[26]M. S. Daw and M. I. Baskes, in *Physics and Chemistry of Fracture,* edited by R. M. Latanison and R. H. Jones (Nijhoff, Dordrecht, 1986).
[27]M. I. Baskes and M. S. Daw, in *Computer Simulation in Materials Science,* edited by R. J. Arsenault, J. Beeler, and D. M. Esterling (American Society for Metals, Metals Park, OH, in press).
[28]M. I. Baskes, S. M. Foiles, and M. S. Daw, J. Phys. (Paris) Colloq. **49**, C5-483 (1988).
[29]S. M. Foiles, Phys. Rev. B **32**, 7685 (1985).
[30]S. M. Foiles, M. S. Daw, and W. D. Wilson, in *High Temperature Alloys: Theory and Design,* edited by J. O. Stiegler (The Metallurgical Society of AIME, New York, 1984).
[31]S. M. Foiles, Phys. Rev. B **32**, 3409 (1985).

[32]K. W. Jacobsen, J. K. Nørskov, and M. J. Puska, Phys. Rev. B **35**, 7423 (1987).
[33]J. K. Nørskov and N. D. Lang, Phys. Rev. B **21**, 2131 (1980).
[34]J. K. Nørskov, Phys. Rev. B **26**, 2875 (1982).
[35]M. W. Finnis and J. E. Sinclair, Philos. Mag. A **50**, 45 (1984).
[36]G. J. Ackland and R. Thetford, Philos. Mag. A **56**, 15 (1987).
[37]R. W. Smith, Ph.D. thesis, The University of Michigan, 1988.
[38]R. W. Smith and G. S. Was, in *Grain Boundary Chemistry and Integranular Fracture,* edited by G. S. Was and S. Bruemmer (Trans Tech, Aedermansdorff, 1989), pp. 199–236.
[39]M. J. Puska, R. M. Nieminen, and M. Manninen, Phys. Rev. B **24**, 3037 (1981).
[40]M. S. Daw, DYN52 source listing, 1985 (unpublished).
[41]M. S. Daw (private communication).
[42]C. S. Barrett and T. B. Massalski, *Structure of Metals* (McGraw-Hill, New York, 1966).
[43]C. J. Smith, *Metals Reference Book,* 5th ed. (Butterworths, London, 1976).
[44]G. Simmons and H. Wang, *Single Crystal Elastic Constants and Calculated Aggregate Properties: A Handbook* (MIT Press, Cambridge, 1971).
[45]P. T. Gallagher and W. A. Oates, Trans. Metall. Soc. AIME **245**, 179 (1969).
[46]J. K. Tien, in *Proceedings of the Third International Conference on Effects of Hydrogen on Behavior of Metals,* edited by I. M. Bernstein and A. W. Thompson (AIME, New York, 1976).
[47]F. Abe and T. Tanabe, Z. Metallkd. **76**, 420 (1985).
[48]W. B. Pearson, *A Handbook of Lattice Spacings and Structures of Metals and Alloy* (Pergamon, New York, 1967).
[49]L. Kaufman, CALPHAD **1**, 7 (1977).
[50]J. T. Lenkkeri, J. Phys. F. **11**, 1991 (1981).
[51]A. Ganrar and U. S. Ghosh, J. Appl. Phys. **52**, 5851 (1981).
[52]C. Kittel, *Introduction to Solid State Physics,* 5th ed. (Wiley, New York, 1976).
[53]A. Seeger, D. Schumacher, W. Schilling, and J. Diehl, *Vacancies and Interstitials in Metals* (North-Holland, Amsterdam, 1970).
[54]K. Christmann, O. Schober, G. Ertl, and M. Neumann, J. Chem. Phys. **60**, 4528 (1974).
[55]K. Christmann, R. J. Behn, G. Ertl, M. A. Van Hohl, and W. H. Weinberg, J. Chem. Phys. **70**, 4168 (1979).
[56]R. M. Kruger (private communication).
[57]*Handbook of Chemistry and Physics,* 61st ed., edited by R. C. Weast (Chemical Rubber Co., Boca Raton, Fl, 1980).
[58]Huntington Alloys, Inconel Alloy 600, 1978.
[59]Huntington Alloys, Inconel Alloy 690 1980.